Observation of Collective Resonance Modes in a Chiral Spin Soliton Lattice with Tunable Magnon Dispersion

Y. Shimamoto,[1,2,*] Y. Matsushima,[1] T. Hasegawa,[1] Y. Kousaka,[1,2] I. Proskurin,[3,4] J. Kishine,[5,6] A. S. Ovchinnikov,[4,7] F. J. T. Goncalves,[8] and Y. Togawa[1,2]

[1]*Department of Physics and Electronics, Osaka Prefecture University, 1-1 Gakuencho, Sakai, Osaka 599-8531, Japan*
[2]*Department of Physics and Electronics, Osaka Metropolitan University, 1-1 Gakuencho, Sakai, Osaka 599-8531, Japan*
[3]*Department of Physics and Astronomy, University of Manitoba, Winnipeg, Manitoba R3T 2N2, Canada*
[4]*Institute of Natural Sciences and Mathematics, Ural Federal University, Ekaterinburg 620002, Russia*
[5]*Division of Natural and Environmental Sciences, The Open University of Japan, Chiba 261-8586, Japan*
[6]*Institute for Molecular Science, Okazaki, Aichi 444-8585, Japan*
[7]*Institute of Metal Physics, Ural Division, Russian Academy of Sciences, Ekaterinburg 620219, Russia*
[8]*Helmholtz-Zentrum Dresden-Rossendorf, Institute of Ion Beam Physics and Materials Research, Bautzner Landstraße 400, 01328 Dresden, Germany*

(Received 2 January 2022; accepted 15 April 2022; published 17 June 2022)

A chiral spin soliton lattice (CSL), one of the representative systems of a magnetic superstructure, exhibits reconfigurability in periodicity over a macroscopic length scale. Such coherent and tunable characteristics of the CSL lead to an emergence of elementary excitation of the CSL as phononlike modes due to translational symmetry breaking and bring a controllability of the dispersion relation of the CSL phonon. Using a broadband microwave spectroscopy technique, we directly found that higher-order magnetic resonance modes appear in the CSL phase of a chiral helimagnet $CrNb_3S_6$, which is ascribed to the CSL phonon response. The resonance frequency of the CSL phonon can be tuned between 16 and 40 GHz in the vicinity of the critical field, where the CSL period alters rapidly. The frequency range of the CSL phonon is expected to extend over 100 GHz as extrapolated on the basis of the theoretical model. The present results indicate that chiral helimagnets could work as materials useful for broadband signal processing in the millimeter-wave band.

DOI: 10.1103/PhysRevLett.128.247203

The presence of a translational symmetry in matter significantly changes the behavior of particles or waves, which are forced to move in a periodic potential. Artificial superlattices or superstructures designed for tailoring the dispersion relation and band structure have made significant advances in functionality in many systems made of photons [1], phonons [2], plasmons [3], and magnons [4]. From a technological point of view, such artificial structures are useful for the device applications aiming at a surface-emitting laser [5], a lowering thermal conductivity [6], a sensitive optical detection of chirality [7], and information processing with magnetic signals [8]. These developments stimulate an ambitious search for tunable structures in periodicity, that are realized in naturally occurring superlattices, such as the chiral spin soliton lattice (CSL) [9,10] and chiral nematic liquid crystals [11,12].

The CSL is a highly reconfigurable and robust superstructure over a macroscopic length scale [10]. The CSL consists of an array of chiral soliton kinks (2π magnetic kinks) periodically partitioned by ferromagnetic domains, as illustrated in Figs. 1(a) and 1(b). The period of the CSL is tunable by altering the strength of an external magnetic field H [9,10]. Thus, the CSL is anticipated to exhibit tunable and reconfigurable magnon dispersion.

The elementary excitation unique to the CSL occurs due to a translational symmetry breaking along the helical axis [13,14]. The kinks of the CSL oscillate collectively around their equilibrium position, which leads to a phononlike excitation of the CSL referred to as a CSL phonon. This means that the Brillouin zone (BZ) is formed in the magnon dispersion depending on the CSL period, as illustrated in Figs. 1(c) and 1(d). Dispersion branches are folded at the BZ boundaries and, in consequence, higher-order modes appear in a broad frequency range. Interestingly, with increasing the CSL period, the size of the BZ becomes smaller and then the frequency gaps between the higher-order modes become narrower. Thus, the CSL phonon modes are expected to have a broad frequency range due to the reconfigurability of the CSL. However, although the spin dynamics of the CSL were investigated in many studies [15–21], the elementary excitations attributed to the CSL phonon have not yet been experimentally observed.

In this Letter, we experimentally demonstrate the existence of the CSL phonon modes in a bulk single crystal of the monoaxial chiral helimagnet $CrNb_3S_6$. Using a

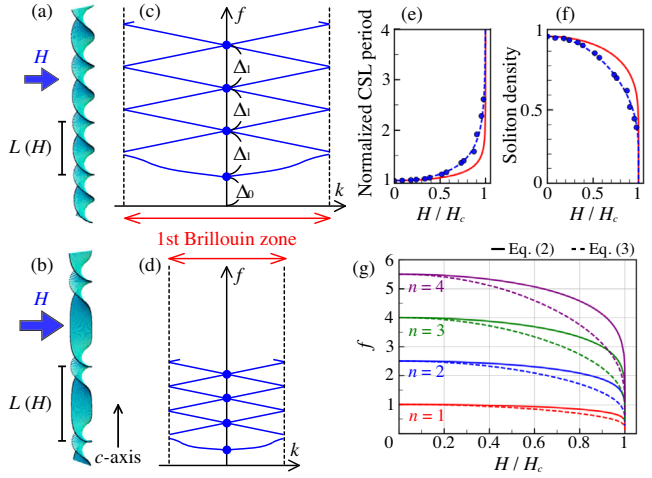

FIG. 1. (a) and (b) Schematic illustrations of a chiral spin soliton lattice (CSL) in the presence of the magnetic field H applied in the direction perpendicular to the c axis of the crystal. The distance between kinks $L(H)$ increases with increasing H. (c),(d) Sketches of the magnon dispersion (frequency f as a function of wave vector k) of the CSL phonon in a reduced Brillouin zone (BZ) scheme. The boundaries (vertical dashed lines) of the BZ are given by $\pi/L(H)$. Blue circles indicate the expected resonance frequencies in the magnetic resonance measurements, where a driving microwave field acts on the sample uniformly ($k \sim 0$). The frequency of the acoustic mode $\Delta_0(H)$ and the frequency gaps between the modes $\Delta_1(H)$ at $k = 0$ are indicated. (e) The normalized CSL period. The solid line shows $L(H)/L(0)$ derived from the 1D chiral sine-Gordon model. The experimental data in Ref. [10] (circles) are fitted by the modified analytical equation $\alpha\{[L(H)/L(0)] - 1\} + 1$ with an empirical parameter $\alpha = 2.3$ (dashed line). (f) The soliton density $L(0)/L(H)$ given in the same manner as the CSL period. (g) The frequency of the CSL phonon as function of H. Solid lines correspond to Eq. (2) with the parameters of $\beta_0 = 1$ and $\beta_1 = 1.5$. Dashed lines are obtained by Eq. (3) with $\alpha = 2.3$, $\beta_0 = 1$, $\beta_1 = 1.5$, and $\gamma = 0$.

broadband microwave spectroscopy technique, we observed multiple resonance modes associated with the CSL phonon response. Higher-order modes grow rapidly from 16 GHz and reach up to 40 GHz, the maximum of which is merely limited by the frequency range available in the instrument used in the present study. According to an analysis of the CSL phonon based on the one-dimensional (1D) chiral sine-Gordon model [13,14], the modes would extend over 100 GHz, which is much higher and broader in frequency than the magnon modes found in conventional ferromagnetic materials. Material parameters characterizing the CSL phonon were obtained for the $CrNb_3S_6$ crystal.

$CrNb_3S_6$ belongs to the space group $P6_322$ and has a layered crystalline structure of 2H-type NbS_2 intercalated by Cr atoms [22]. The Cr atoms have localized electrons with spins of $S_{\rm spin} = 3/2$. An antisymmetric exchange interaction, frequently referred to as a Dzyaloshinskii-Moriya (DM) interaction D [23,24], competes with a Heisenberg symmetric exchange interaction J along the principal axis of the crystal (c axis), resulting in the emergence of chiral helimagnetic (CHM) order as a ground state at zero field below a critical temperature T_c. A helical pitch of the CHM state L_0 is determined by the ratio between the magnitudes of J and D. In the case of $CrNb_3S_6$, L_0 was observed as 48 nm, which allows an estimation of D/J to be approximately 0.16 [10]. An individual estimation of J and D would be useful for further understanding fundamental properties of chiral magnetic materials.

When H is applied in the direction perpendicular to the c axis, the harmonic CHM state transforms to the nonlinear CSL. The CSL period $L(H)$ grows with increasing H below a critical field H_c, as shown in Figs. 1(a) and 1(b). With increasing H above H_c, the CSL is saturated and transforms to a forced-ferromagnetic (F-FM) state. Note that the CSL formation is described analytically by the 1D chiral sine-Gordon model [9,10]. This model gives $L(H)/L(0) = 4K(\kappa)E(\kappa)/\pi^2$, as indicated by a solid line in Fig. 1(e), where $K(\kappa)$ and $E(\kappa)$ are elliptic integrals of the first and second kind with an elliptic modulus κ, respectively. However, the experimental data of $L(H)$ obtained by using Lorentz microscopy [10] (indicated by circles), exhibits a looser variation with regards to H than that expected for the analytical model. Consequently, an introduction of the prefactor α is required for making a fitting of the experimental data, and then, $L(H)/L(0)$ is modified as $\alpha\{[L(H)/L(0)] - 1\} + 1$. The soliton density $L(0)/L(H)$, which plays the role of an order parameter of the CSL formation, is modified into $(\alpha\{[L(H)/L(0)] - 1\} + 1)^{-1}$, as shown in Fig. 1(f).

Bulk single crystals of $CrNb_3S_6$ were grown using a chemical vapor transport method [25]. The crystal used in the present study has a platelet shape of the c plane, with an area of approximately 1.1 mm^2 and a length of 0.2 mm along the c axis. T_c of 132 K was observed in magnetization measurements, which is consistent with the values reported in the literature [26].

A microwave circuit, consisting of a coplanar waveguide (CPW) connected to a two-port vector network analyzer (VNA), was used to detect magnetic resonance signals. Details of the experimental setup can be found elsewhere [16,17,19,20]. The CPW is made of 18 μm thick copper with a gold coating on the dielectric substrate. The signal line is 100 μm in width, with an edge-to-edge gap of 50 μm to the ground lines, which have a width of 400 μm. A driving microwave field, which is supplied into the CPW from the VNA, circulates the signal line and is confined in the gap region against the ground lines. The in-plane component of the microwave field dominantly excites the magnetic resonance in the sample located on top of the CPW. The crystal was placed over the signal line so that its c axis orients in the direction normal to the substrate. A skin depth of 1.8 μm was estimated based on the $CrNb_3S_6$ crystal, at a frequency of 20 GHz. This depth allows us to excite up to 40 kinks at zero field.

A scattering parameter S_{para} for the microwave transmission from the port 2 to port 1 of the VNA is measured as a function of frequency at various strengths of H. The frequency sweep is set between 1 and 40 GHz, with steps of 30 MHz. The maximum frequency is limited by the VNA available in our laboratory. The resonance properties at fixed frequencies in swept H are also examined.

Figure 2(a) shows an intensity plot of the field derivative of the resonance amplitude [27] as a function of frequency and field. The data was taken by frequency sweep measurements performed at each step of H, while being varied from +200 mT to −200 mT in steps of 1 mT. H is applied in the direction perpendicular to both the c axis and the microwave field. The sample was cooled down to 100 K using liquid nitrogen. At this temperature, the transition between the CSL and F-FM phases occurs at H_c of 181 mT.

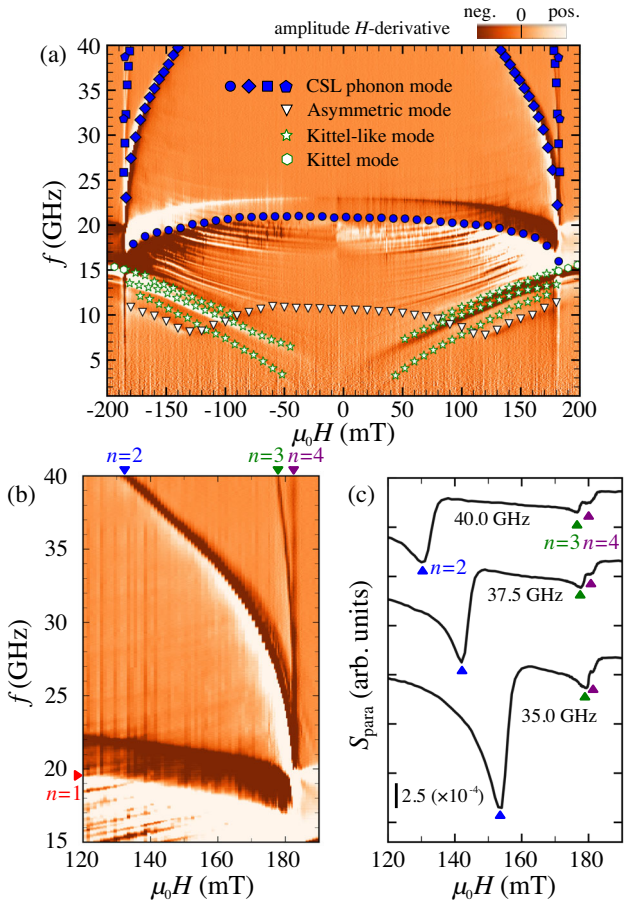

FIG. 2. The magnetic resonance data of the bulk single crystal of $CrNb_3S_6$ at a temperature of 100 K. (a) The resonance frequency as a function of H in an intensity plot of the field derivative of the resonance amplitude [27]. The color contrast (arbitrary unit) represents the detection of the resonance. (b) An enlarged view of the CSL phonon modes. The lowest frequency mode ($n = 1$) and three higher-order modes ($n = 2$, 3, and 4) are identified. (c) Line traces of S_{para} as a function of H at various frequencies. The resonance peaks of $n = 2$, 3, and 4 modes are detected. The vertical line is a scale bar for the magnitude of S_{para} (linear scale).

Three types of the resonance modes in the CSL phase are identified based on the H dependence of resonance frequency. The first noticeable feature is that multiple resonance modes were observed above 16 GHz, as indicated by solid markers. The resonance frequency in all the modes decreases with increasing the strength of H and converges toward H_c. Such dome-shaped characteristics of the resonance frequency are similar to that derived from the analytical calculation [13,14] of the CSL phonon, as shown in Fig. 1(g).

A second type of a resonance mode, referred to as an asymmetric mode, appears between 7.8 and 11.4 GHz, as indicated by downward triangles. This mode is characterized by the asymmetric behavior of the resonance frequency with regards to zero field, as discussed in the previous studies [16,17,19–21,28]. Indeed, a linear dependence of the resonance frequency across zero magnetic field is observed between +80 and −60 mT.

A third type of resonance mode, referred to as a Kittel-like mode, appears in the low frequency regime and shows a monotonous increase of the resonance frequency with regards to the strength of H, as indicated by stars. This mode is naturally connected to the one in the F-FM phase, which is ascribed to the Kittel mode observed in conventional ferromagnetic materials. Thus, it is regarded as the contribution from the ferromagnetic domains that partition the kinks in the CSL.

Hereafter, we focus on the multiple resonance modes above 16 GHz. Figure 2(b) shows the close-up spectra in the vicinity of H_c. Four resonance branches are numbered as $n = 1$, 2, 3, and 4, respectively. The $n = 2$, 3, and 4 modes clearly appear up to 40 GHz.

These higher-order modes are detectable even in the H sweep measurements at a fixed frequency, as shown in Fig. 2(c). The resonance peaks corresponding to the $n = 2$, 3, and 4 modes are found at 35.0, 37.5, and 40.0 GHz, respectively. The $n = 1$ mode decreases in resonance amplitude with increasing the strength of H, as shown in Fig. 3(a). On the other hand, the resonance amplitude for $n \geqq 2$ modes increases when H approaches H_c. We will discuss the H dependence of the amplitude for all the modes afterwards.

Let us compare the experimental data of the multiple resonance modes with the analytical solution of the CSL phonon [13,14]. According to the analytical model, the dispersion relation of the CSL phonon consists of acoustic and optical modes, as shown in Fig. 1(c). The former appears at the lowest frequency with a finite frequency gap $\Delta_0(H)$ at a wave vector $k = 0$, while the latter shows multiple higher-order modes with a gap $\Delta_1(H)$. In the CSL system, $\Delta_0(H)$ originates from the DM interaction and works as a potential to confine the directions of the spin within the c plane, which contrasts with a gapless feature of an acoustic phonon in the crystal lattice. $\Delta_0(H = 0)$ is

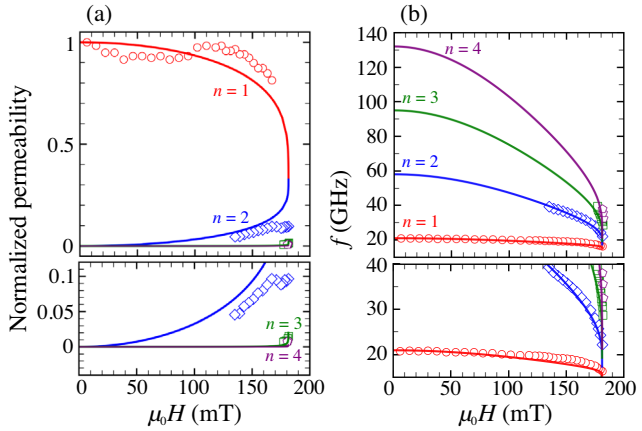

FIG. 3. The analysis of the CSL phonon modes. (a) The amplitude of the $n = 1$, 2, 3, and 4 modes as a function of H. The experimentally obtained magnetic permeability $ln[S^{res}_{para}/S^{ref}_{para}]/ln[S^{ref}_{para}]$ (markers) and the theoretically obtained magnetic susceptibility of the CSL phonon modes (continuous lines) are compared qualitatively. The details of the analytical equations are available in Ref. [14]. (b) The resonance frequency of the $n = 1$, 2, 3, and 4 modes. The continuous lines correspond to a fit to Eq. (3) at $\alpha = 4.7$, $\beta_0 = 5.9$ GHz, $\beta_1 = 37$ GHz, and $\gamma = 15.0$ GHz.

given analytically by $D^2S^2_{spin}/2J$ [29,30], while $\Delta_1(H = 0)$ is $DS^2_{spin}/2$ [13]. Thus, a data fitting of the CSL phonon would allow an estimation of D and J in the crystal.

First, it is necessary to experimentally identify the acoustic and optical modes of the CSL phonon. In the analytical calculation, the acoustic and optical modes are distinguishable in terms of the H dependence of the magnetic susceptibility [14]. When H approaches H_c, the magnetic susceptibility for the acoustic mode decreases, while those for the optical modes increase. The details of analytical equations for the magnetic susceptibility of the CSL phonon are available in Ref. [14]. For comparison, the magnitude of S_{para} is transformed into a magnetic permeability μ through the relation $\mu \simeq ln[S^{res}_{para}/S^{ref}_{para}]/ln[S^{ref}_{para}]$, where S^{res}_{para} is an on-resonance spectrum and S^{ref}_{para} is a reference one [31]. The resonance amplitude in the experiment can be compared qualitatively with theoretical equations because the magnetic permeability is proportional to the magnetic susceptibility.

Figure 3(a) shows the normalized magnetic permeability of multiple resonance modes. Experimentally, the amplitude of the $n = 1$ mode is relatively large and exhibits the H dependence which differs from those for the $n = 2$, 3, and 4 modes. The data of the $n = 1$ mode above 177 mT are not evaluated exactly because the mode overlaps with the Kittel mode in the F-FM phase. With an assumption of the acoustic mode as the origin of $n = 1$ mode, the H dependence of the magnetic susceptibility obtained analytically [14] becomes qualitatively similar to the experimental data of μ. This finding supports that the $n = 1$ mode corresponds to the acoustic mode of the CSL phonon, while the $n \geqq 2$ modes are ascribed to the optical modes. The observed behavior is consistent with a general tendency of evolution of various harmonics of the CSL structure upon the magnetic field increase, as shown in Figs. 24 and 25 in Ref. [32]. Namely, this observation is a manifestation of nonlinear spatial structure of the CSL.

The resonance frequency of the CSL phonon $f_n(H)$ is expressed approximately as follows [14]:

$$f_n(H) \simeq 2\pi \frac{L(0)}{L(H)} n. \tag{1}$$

The frequency of the CSL phonon modes is simply proportional to the soliton density $L(0)/L(H)$ shown in Fig. 1(f). We normalize Eq. (1) for clarity and introduce two parameters β_0 and β_1 to determine the energy scales of $\Delta_0(0)$ and $\Delta_1(0)$ individually,

$$f_n(H) = \frac{L(0)}{L(H)}[(n-1)\beta_1 + \beta_0]. \tag{2}$$

Equation (2) for $n = 1$, 2, 3, and 4 at $\beta_0 = 1$ and $\beta_1 = 1.5$ is indicated by solid lines in Fig. 1(g). β_0 is the frequency of the acoustic mode at zero field, while β_1 is the frequency difference between optical modes at zero field.

The empirical parameter α should be introduced to the analysis for the CSL phonon in the same manner as that for the CSL period [10], as explained above. Consequently, Eq. (2) is reformulated into the following equation by the use of modified soliton density $(\alpha\{[L(H)/L(0)]-1\}+1)^{-1}$ instead of $L(0)/L(H)$:

$$f_n(H) = \frac{(n-1)\beta_1 + \beta_0}{\alpha[\frac{L(H)}{L(0)} - 1] + 1} + \gamma. \tag{3}$$

Dashed lines in Fig. 1(g) show Eq. (3) at $\alpha = 2.3$, $\beta_0 = 1$, $\beta_1 = 1.5$, and $\gamma = 0$.

Here, the parameter γ is introduced as a frequency offset and corresponds to the resonance frequency of all the CSL phonon modes at H_c. In theory, this point should start from zero [13,14]. However, in the experiment, the resonance frequency at H_c is found to be 15.0 GHz as it connects continuously to the resonance mode attributed to the F-FM phase. The frequency offset related to the resonance characteristics is required for reproducing the experimental data.

The term β_0 is determined as 5.9 GHz by the resonance frequency of the $n = 1$ mode at zero field, which is experimentally obtained as 20.9 GHz. β_0 governs $\Delta_0(0)$, which is given analytically by $D^2S^2_{spin}/2J$ [29,30]. Thus, β_0 allows the estimations of D and J in the crystal by using $D/J = 0.16$ [10]. In consequence, 3.4 K is obtained for D, while 21 K for J with the parameter of $S_{spin} = 1.02$, estimated by the saturation magnetization at the temperature of 100 K (not shown).

The term β_1 governs $\Delta_1(0)$, which scales to the magnitude of D as given by $DS_{\mathrm{spin}}^2/2$ [13]. β_1 is obtained as 37 GHz with $D = 3.4$ K and $S_{\mathrm{spin}} = 1.02$.

Eventually, the empirical parameter α remains as a fit parameter for Eq. (3). Figure 3(b) shows the experimentally obtained resonance frequency plotted together with Eq. (3) for $n = 1, 2, 3$, and 4. A good agreement is obtained when using the parameter as 4.7 for α.

As for the value of α, our observations using Lorentz microscopy clarified that α took different values in several thin platelet samples of the $CrNb_3S_6$ crystals. Although the physical meaning of α is still unclear, the present resonance measurements could offer the possibility to evaluate α directly in the bulk samples. Thus, we could investigate α values from various viewpoints such as the crystal quality and size. We leave this interesting issue for future work.

Let us discuss the validation of the magnitude of D and J obtained in the $CrNb_3S_6$ crystals. H_c could be provided by using the magnitude of D and J. Based on the 1D chiral sine-Gordon model, H_c is given analytically by $H_c \simeq \pi^2 D^2 S_{\mathrm{spin}}/16J$ [33,34]. With $D = 3.4$ K, $D/J = 0.16$, and $S_{\mathrm{spin}} = 1.02$, H_c is estimated to be 255 mT, which should be compared with the value of 181 mT obtained in the experiment. A discrepancy may be caused by one dimensionality of the theoretical model of the CSL phonon, in which the exchange interaction between the helical chains $J_\perp$ is ignored.

The frequency range of the CSL phonon observed in our experiments is rather broad and high, compared to that of conventional ferromagnetic materials, especially in the low H regime. Indeed, the resonance frequencies of higher-order modes vary from 16 and 40 GHz within a small H change of 50 mT for $n = 2$, of 6 mT for $n = 3$, and of 3 mT for $n = 4$. When extrapolating the data using the analytical solution, $n \geq 4$ modes are expected to extend over 100 GHz, as shown in Fig. 3(b).

The CSL phonon modes would appear in other chiral magnetic materials hosting the CSL, such as a monoaxial $YbNi_3Al_9$ [35,36] and $CrTa_3S_6$ [37,38]. The resonance frequency can be estimated by using their material parameters. In the case of $CrTa_3S_6$ single crystal, $\Delta_1(0)$ and $\Delta_0(0)$ are calculated as 130 GHz and 40 GHz, respectively, using the parameters in Ref. [37]. Thus, the frequency band will reach sub-THz regime in higher-order modes. Even in cubic B20-type chiral crystals, the CSL phase would appear as the ground state upon application of a tensile strain [39]. Therefore, there are many material choices that would exhibit the CSL phonon. We stress that the CSL phonon originates from the periodic and coherent nature of the CSL. Consequently, the frequency can be tuned over a wide range due to the tunable and reconfigurable dispersion of the CSL phonon. We believe that these findings offer novel perspectives on the reconfigurable band structure in other wave phenomena.

We would like to thank T. Arakawa for the technical support in the fabrication of the CPW. We also appreciate fruitful discussions with M. Hagiwara, Y. Sawada, Y. Kato, T. Sato, K. Matsumoto, and J. Ohe. We acknowledge D. Yoshizawa, S. Tajima, K. Inoue and M. Mito for the experiments performed in the early stage. This work was financially supported by Japan Society for the Promotion of Science (JSPS) through Grants-in-Aid for Scientific Research (B) (No. JP17H02767) and on Innovative Areas "Quantum Liquid Crystals" (No. JP19H05826). This work was also supported by Research Grant of Specially Promoted Research Program from Toyota Physics and Chemical Research Institute. The research funding from the Ministry of Science and Higher Education of the Russian Federation (Ural Federal University Program of Development within the Priority-2030 Program) is gratefully acknowledged. A. S. O. thanks the Russian Foundation for Basic Research (RFBR), Grant No. 20-52-50005, and the Ministry of Science and Higher Education of the Russian Federation, project No. FEUZ-2020-0054. Y. S. was supported by Research Fellowships of JSPS for Young Scientists (No. 21J14431) and Graduate Course for System-inspired Leaders in Material Science of JSPS.

*y-shimamoto-omu@omu.ac.jp

[1] E. Yablonovitch, Inhibited Spontaneous Emission in Solid-State Physics and Electronics, Phys. Rev. Lett. **58**, 2059 (1987).

[2] I. E. Psarobas, N. Stefanou, and A. Modinos, Scattering of elastic waves by periodic arrays of spherical bodies, Phys. Rev. B **62**, 278 (2000).

[3] S. C. Kitson, W. L. Barnes, and J. R. Sambles, Full Photonic Band Gap for Surface Modes in the Visible, Phys. Rev. Lett. **77**, 2670 (1996).

[4] S. A. Nikitova, Ph. Tailhadesa, and C. S. Tsai, Spin waves in periodic magnetic structures—magnonic crystals, J. Magn. Magn. Mater. **236**, 320 (2001).

[5] M. Imada, S. Noda, A. Chutinan, and T. Tokuda, Coherent two-dimensional lasing action in surface-emitting laser with triangular-lattice photonic crystal structure, Appl. Phys. Lett. **75**, 316 (1999).

[6] J.-K. Yu, S. Mitrovic, D. Tham, J. Varghese, and J. R. Heath, Reduction of thermal conductivity in phononic nanomesh structures, Nat. Nanotechnol. **5**, 718 (2010).

[7] E. Hendry, T. Carpy, J. Johnston, M. Popland, R. V. Mikhaylovskiy, A. J. Lapthorn, S. M. Kelly, L. D. Barron, N. Gadegaard, and M. Kadodwala, Ultrasensitive detection and characterization of biomolecules using superchiral fields, Nat. Nanotechnol. **5**, 783 (2010).

[8] A. V. Chumak, A. A. Serga, and B. Hillebrands, Magnon transistor for all-magnon data processing, Nat. Commun. **5**, 4700 (2014).

[9] I. E. Dzyaloshinsky, Theory of helicoidal structures in antiferromagnets. I. Nonmetals, Sov. Phys. JETP **19**, 960 (1964).

[10] Y. Togawa, T. Koyama, K. Takayanagi, S. Mori, Y. Kousaka, J. Akimitsu, S. Nishihara, K. Inoue, A. S. Ovchinnikov, and J. Kishine, Chiral Magnetic Soliton Lattice on Chiral Helimagnet, Phys. Rev. Lett. **108**, 107202 (2012).

[11] K. Yoshino, Y. Shimoda, Y. Kawagishi, K. Nakayama, and M. Ozaki, Temperature tuning of the stop band in transmission spectra of liquid-crystal infiltrated synthetic opal as tunable photonic crystal, Appl. Phys. Lett. **75**, 932 (1999).

[12] H. J. Coles and M. N. Pivnenko, Liquid crystal 'blue phases' with a wide temperature range, Nature (London) **436**, 997 (2005).

[13] J. Kishine and A. S. Ovchinnikov, Theory of spin resonance in a chiral helimagnet, Phys. Rev. B **79**, 220405(R) (2009).

[14] V. V. Kiselev and A. A. Raskovalov, Standing spin waves and solitons in a quasi-one-dimensional spiral structure, J. Exp. Theor. Phys. **116**, 272 (2013).

[15] F. B. Mushenok, Ferromagnetic resonance in the $CrNb_{1/3}S_2$ helical magnet, Phys. Solid State **55**, 2482 (2013).

[16] F. J. T. Goncalves, T. Sogo, Y. Shimamoto, Y. Kousaka, J. Akimitsu, S. Nishihara, K. Inoue, D. Yoshizawa, M. Hagiwara, M. Mito, R. L. Stamps, I. G. Bostrem, V. E. Sinitsyn, A. S. Ovchinnikov, J. Kishine, and Y. Togawa, Collective resonant dynamics of the chiral spin soliton lattice in a monoaxial chiral magnetic crystal, Phys. Rev. B **95**, 104415 (2017).

[17] F. J. T. Goncalves, T. Sogo, Y. Shimamoto, I. Proskurin, V. E. Sinitsyn, Y. Kousaka, I. G. Bostrem, J. Kishine, A. S. Ovchinnikov, and Y. Togawa, Tailored resonance in micrometer-sized monoaxial chiral helimagnets, Phys. Rev. B **98**, 144407 (2018).

[18] D. Yoshizawa, Y. Sawada, Y. Kousaka, J. Kishine, Y. Togawa, M. Mito, K. Inoue, J. Akimitsu, T. Nakano, Y. Nozue, and M. Hagiwara, Anomalous spiked structures in ESR signals from the chiral helimagnet $CrNb_3S_6$, Phys. Rev. B **100**, 104413 (2019).

[19] Y. Shimamoto, F. J. T. Goncalves, T. Sogo, Y. Kousaka, and Y. Togawa, Switching behavior of the magnetic resonance in a monoaxial chiral magnetic crystal $CrNb_3S_6$, Appl. Phys. Lett. **115**, 242401 (2019).

[20] F. J. T. Goncalves, Y. Shimamoto, T. Sogo, G. W. Paterson, Y. Kousaka, and Y. Togawa, Field driven recovery of the collective spin dynamics of the chiral soliton lattice, Appl. Phys. Lett. **116**, 012403 (2020).

[21] Y. Shimamoto, F. J. T. Goncalves, T. Sogo, Y. Kousaka, and Y. Togawa, Anisotropic microwave propagations in a reconfigurable chiral spin soliton lattice, Phys. Rev. B **104**, 174420 (2021).

[22] T. Miyadai, K. Kikuchi, H. Kondo, S. Sakka, M. Arai, and Y. Ishikawa, Magnetic properties of $Cr_{1/3}NbS_2$, J. Phys. Soc. Jpn. **52**, 1394 (1983).

[23] I. E. Dzyaloshinsky, A thermodynamic theory of "weak" ferromagnetism of antiferromagnetics, J. Phys. Chem. Solids **4**, 241 (1958).

[24] T. Moriya, Anisotropic superexchnage interaction and weak ferromagnetism, Phys. Rev. **120**, 91 (1960).

[25] Y. Kousaka, Y. Nakao, J. Kishine, M. Akita, K. Inoue, and J. Akimitsu, Chiral helimagnetism in $T_{1/3}NbS_2$ (T = Cr and Mn), Nucl. Instrum. Methods Phys. Res., Sect. A **600**, 250 (2009).

[26] Y. Togawa, Y. Kousaka, S. Nishihara, K. Inoue, J. Akimitsu, A. S. Ovchinnikov, and J. Kishine, Interlayer Magnetoresistance due to Chiral Soliton Lattice Formation in Hexagonal Chiral Magnet $CrNb_3S_6$, Phys. Rev. Lett. **111**, 197204 (2013).

[27] The resonance amplitude are obtained by subtracting a background spectrum $S^{\mathrm{ref}}_{\mathrm{para}}$ from the on-resonance data $S^{\mathrm{res}}_{\mathrm{para}}$, in order to remove unwanted nonmagnetic losses of the circuit. The field derivative of the resonance amplitude is useful for identifying the resonance modes that depend on H.

[28] J. Kishine, Vl. E. Sinitsyn, I. G. Bostrem, I. Proskurin, F. J. T. Goncalves, Y. Togawa, and A. S. Ovchinnikov, Theory of standing spin waves in a finite-size chiral spin soliton lattice, Phys. Rev. B **100**, 024411 (2019).

[29] I. G. Bostrem, J. Kishine, and A. S. Ovchinnikov, Transport spin current driven by the moving kink crystal in a chiral helimagnet, Phys. Rev. B **77**, 132405 (2008).

[30] I. G. Bostrem, J. Kishine, and A. S. Ovchinnikov, Theory of spin current in chiral helimagnets, Phys. Rev. B **78**, 064425 (2008).

[31] S. S. Kalarickal, P. Krivosik, M. Z. Wu, C. E. Patton, M. L. Schneider, P. Kabos, T. J. Silva, and J. P. Nibarger, Ferromagnetic resonance linewidth in metallic thin films: Comparison of measurement methods, J. Appl. Phys. **99**, 093909 (2006).

[32] J. Kishine and A. S. Ovchinnikov, Theory of monoaxial chiral helimagnet, Solid State Phys. **66**, 1 (2015).

[33] J. Kishine, A. S. Ovchinnikov, and I. V. Proskurin, Sliding conductivity of a magnetic kink crystal in a chiral helimagnet, Phys. Rev. B **82**, 064407 (2010).

[34] M. Shinozaki, S. Hoshino, Y. Masaki, J. Kishine, and Y. Kato, Finite-temperature properties of three-dimensional chiral helimagnets, J. Phys. Soc. Jpn. **85**, 074710 (2016).

[35] S. Ohara, T. Yamashita, Y. Mori, and I. Sakamoto, Transport and magnetic properties of new heavy-fermion antiferromagnet $YbNi_3Al_9$, J. Phys. Conf. Ser. **273**, 012048 (2011).

[36] H. Shishido, A. Okumura, T. Saimyoji, S. Nakamura, S. Ohara, and Y. Togawa, Thin film growth of heavy fermion chiral magnet $YbNi_3Al_9$, Appl. Phys. Lett. **118**, 102402 (2021).

[37] C. Zhang *et al.*, Chiral helimagnetism and one-dimensional magnetic solitons in a Cr-intercalated transition metal dichalcogenide, Adv. Mater. **33**, 2101131 (2021).

[38] D. Obeysekera, K. Gamage, Y. Gao, S.-w. Cheong, and J. Yang, The magneto-transport properties of $Cr_{1/3}TaS_2$ with chiral magnetic solitons, Adv. Electron. Mater. **7**, 2100424 (2021).

[39] V. Ukleev, Y. Yamasaki, O. Utesov, K. Shibata, N. Kanazawa, N. Jaouen, H. Nakao, Y. Tokura, and T. Arima, Metastable solitonic states in the strained itinerant helimagnet FeGe, Phys. Rev. B **102**, 014416 (2020).